

1 **NOMENCLATURE**

2

3	CHF	Critical Heat Flux
4	BS	Bare Surface
5	NPDS	Nanoparticle Deposited Surface
6	HPP	Honeycomb Porous Plate
7	HSP	Honeycomb Solid Plate
8	PWR	Pressurized Water Reactors
9	RPV	Reactor Pressure Vessel
10	IVR	In-Vessel Retention
11	TC	Thermocouple
12	k	thermal conductivity (W/m·K)
13	c	specific heat (J/g·K)
14	T	temperature (K)
15	d_v	HPP channel width (m)
16	δ_s	HPP wall thickness (m)
17	δ_s	HPP height (m)
18	ρ	density (kg/m ³)

19

20 **Subscripts**

21	L	liquid
22	S	solid

23

24

25

1. INTRODUCTION

Quenching refers to the rapid cooling of a hot object by exposing it to a cooler liquid. When a liquid and a solid with a large temperature difference between them are brought into contact, a vapor film that prevents direct solid-liquid contact is formed, such regime is known as film boiling. As the temperature decreases due to heat transfer through this vapor film, it becomes unstable and the heat transfer rate increases significantly due to local solid-liquid contact. Eventually, the vapor film vanishes and transition to nucleate boiling occurs, which is the desired working condition since it provides the highest heat transfer rates.

One of the applications for the current study is on in-vessel retention (IVR) of pressurized water reactors (PWR), which is a countermeasure in the event of a severe accident accompanied by nuclear fuel meltdown. In this situation, IVR, which involves external cooling of the reactor pressure vessel (RPV) to remove the decay heat from the melting core, is employed in order to assure the confinement of the molten fuel in the RPV. Recently, this technique has attracted attention as a new accident management strategy [1].

When cooling the RPV, it is important to accelerate the transition from film boiling to nucleate boiling, a much more efficient boiling regime, in order to avoid the RPV structural failure. Numerous studies with this purpose have been reported. Fan et al. [2] modified the surface of stainless steel spheres to investigate the effect of surface wettability on the cooling rate in saturated water at atmospheric pressure. It was found that the cooling period of super-hydrophilic spheres were 7 s shorter than that of original clean spheres due to reduced film boiling period. Kang et al. [3] found that the heat transfer coefficient was significantly increased by capillary wicking and the use of a completely wettable surface (contact angle near to 0) produced by oxidation to form nano-pins.

In addition, using metal spheres, Sher et al. [4] clarified the effect of factors such as the type of metal, sphere diameter, and degree of sub-cooling on quenching. Shahriari et al. [5] found that the

vapor film disappeared at higher temperatures when a voltage was applied between the liquid and the heat-transfer surface.

Additionally, Hsu et al. [6] compared quenching of stainless steel 304 and zircaloy-702 spheres in natural seawater and de-ionized water. They suggested that the formation of the vapor film was inhibited in seawater by the zeta-potential effect and thus this fluid provided a much shorter quenching time. Moreover, high speed camera images of the boiling phenomena on both spheres were used to support their conclusion.

Furthermore, studies have reported increasing in cooling rate by depositing a thin uniform layer of nanoparticles on the heat-transfer surface [7–10]. For example, Kim et al. [11] pointed out that deposition of a nanoparticle layer destabilizes the formation of a vapor film, thereby facilitating liquid-solid contact locally, resulting in rapid cooling.

Another important requirement for IVR is improving the critical heat flux (CHF). Mori et al. recently proposed a CHF enhancement technique that involves attaching an HPP, which has pores for supplying liquid by capillary action and cells through which the vapor escapes from the heated surface [12–15]. They also showed that quenching could be enhanced by attaching an HPP to a copper cylinder [16].

However, to apply these methods to IVR, it is necessary to consider the physical properties of the high-temperature body itself. Moreover, the quenching enhancement mechanism is not yet fully understood. Therefore, in the present study, we performed experiments using a high-temperature rod made of stainless steel, whose properties are similar to those of a RPV, and examined the details of the boiling mechanism using a high-speed camera. The effect of an HPP attachment and a nanoparticle deposited surface (NPDS) on quenching of the stainless-steel rod in distilled water at saturation temperature were also studied. Although in a real IVR scenario the coolant is in

subcooled condition, the experiments were conducted in saturated condition. Film boiling is not detected in subcooled condition. Thus, in order to analyze film boiling regime on different surface conditions, saturated quenching was evaluated. Furthermore, since subcooled quenching is known to have a better performance than that of saturated [17], the results presented here represent the worst possible scenario in an accident situation.

2. EXPERIMENTAL APPARATUS AND PROCEDURE

2.1 Experimental apparatus

Figure 1 shows a schematic diagram of the quenching test facility. The vertical SUS304 stainless steel test rod was 115 mm long and 40 mm in diameter. In order to reduce the edge effect on quenching, the corners of the rod close to its lower end were chamfered at R5 mm resulting in a test surface of 30 mm in diameter. The temperature of the rod at 10 mm from the heated surface was monitored through a K-type sheath thermocouple (TC1).

<Figure 1>

The pool container was made of Pyrex glass and filled with distilled water, which temperature was measured with another thermocouple (TC2). The liquid was maintained at its saturation temperature using a 0.5-kW immersion heater. To keep water level constant, the pool was connected to a water reservoir. It made possible the injection of liquid at saturated temperature into the pool, keeping it completely filled during quenching. Before the experiment, the rod and the pool were carefully positioned so that, after the pool was filled, the heated surface was submerged 1 mm into the liquid. Both the rod and the pool were kept still and thermally insulated to avoid heat losses during the experiments. The thermocouples were connected to a digital recorder and monitored at sampling frequency of 200 Hz. The boiling mechanism could be observed from the bottom of the pool through a high-speed camera and a mirror.

The HPP used in the present study, fabricated from CaOAl_2O_3 (30–50 wt%), fused silicon dioxide (SiO_2) (40–60 wt%), and TiO_2 (5–20 wt%), is shown in Figure 2. An optical micrograph of its structure can be seen on the right side of the figure. The vapor escape channel width (cell width), grid wall thickness, aperture ratio (ratio of the open area to the total area), HPP height, and diameter were $d_V = 1.3$ mm, $\delta_S = 0.4$ mm, 0.55, $\delta_h = 10$ mm, and 30.0 mm, respectively. A honeycomb solid plate (HSP) with no pores was also used during the experiments. It was fabricated by impregnating an HPP with repellent to completely suppress capillary action.

<Figure 2>

2.2 Experimental procedures

The stainless-steel rod was heated by cartridge heaters inserted into its upper end. When the registered temperature at TC1 position (10 mm from the test surface) was approximately 623 K, the valve of the reservoir was opened raising the level of water in the pool, overflowing it. At this configuration, the heated surface remained immersed approximately 1 mm into the distilled water. Heating was stopped at the moment the rod made contact with the water. The same process was repeated for all cases. Although the positions of the rod and the pool were accurately set for each run, the depth of the surface in the coolant could only be assure during film boiling, when fluctuation in the water level was minimal. In nucleate boiling regime, the coolant surface varied considerably due to the turbulence caused by the large number of bubbles formed on the heated surface. Since it was not possible to precisely determine the depth of the surface during the latter regime, this work focused on the film boiling as the most import regime in the analysis of the quenching times.

The nanoparticle used in the present study was TiO_2 powder made from Aeroxide TiO_2 P 25 by Evonik Corporation. The mean size of the dry nanoparticles was supplied by the manufacturer as 21 nm. To produce the NPDS surface, water-based nanofluid with concentration of 0.1 vol.% (4

g/L) was prepared by dispersing dry nanoparticle powder in distilled water and then subjecting the suspension to ultrasonic vibration for 2 h. Thus, a preliminary quenching experiment using this nanofluid was performed. Although no additives such as surfactants or dispersants were used to stabilize the nanoparticle suspension, it has proved to be stable. Analysis of particle diameter distribution before and after the experiment, using a Laser Diffraction Particle Size Analyser (SALD-7000) from Shimadzu, revealed the absence of particles clustering. The mean particle diameter were 197 ± 8 nm and 188 ± 8 nm before and after quenching respectively. Furthermore, sedimentation of nanoparticles was not detected.

Surface temperature calculated by solving the inverse problem presented poor accuracy due to the small thermal diffusivity of the SUS rod (4×10^{-6} m²/s) and the distance of TC1 from the surface. Thus, the TC1 temperature as function of time and $-dT/dt$ were evaluated in the present study. The quench time was defined as the time from the initial immersion of the high-temperature rod to the time when $-dT/dt$ reached its maximum value.

The uncertainty in temperatures values was 0.5 K and for electrical resistance was approximately 1 % of the measured value. Due to deviation of the experimental data, the relative uncertainties for the quenching time varied from 3 % to until 20 % and for $-dT/dt$ it was of 16 % of the calculated value. Although these values may seem large, the difference of the obtained quenching times were enough to differentiate the performance of the surfaces tested.

3. EXPERIMENTAL RESULTS AND DISCUSSION

Figures 3 compares (a) quenching curves and (b) $-dT/dt$ as a function of the temperature at TC1 position for the BS, an HPP, and a HSP. Although at least three runs were performed in each case, the curves shown are from one single run and were chosen as representative of all data based on its quenching time. Just after the heated rod was immersed in distilled water a vapor film is formed on the heated surface and its temperature decreases slowly due to the low thermal conductivity of

the vapor. Next, solid-liquid contact begins to occur locally due to vapor film instability, initiating the transition to nucleate boiling.

The average quench time on the BS case was 1380 ± 112 s, while with an HPP it was 304 ± 48 s, nearly 6-times smaller. In addition, when the HSP was employed, which is exactly as an HPP but with no pores, the quench time was approximately 522 ± 49 s. The comparison of the HPP and HSP quenching times indicates that the supply of liquid through capillary action, provided by the pores in the HPP walls, is an important factor for cooling performance of the rod and so the shorter time observed.

<Figure 3>

In the case of the BS, film boiling occurs up to approximately 1200 s then the regime changes to nucleate boiling. During film boiling on the BS, the vapor film covers the heated surface, and steam escapes from its edges. In the case of the HPP, the generated steam frequently escapes through the channels as large bubbles, even before the nucleate-boiling regime. Bubble detachment frequency in this regime was approximately 4 Hz. Additionally, when nucleate-boiling regime, boiling was more vigorously and bubbles detached at average frequency of approximately 10 Hz. Figure 4 presents images of quenching experiment with the HPP showing the criteria adopted for bubbles departure frequency calculation. In these images, each cycle corresponds to one bubble departure. To help in distinguishing subsequent cycles, different bubbles were colored in red, blue and green.

<Figure 4>

It is interesting to note that $-dT/dt$ with the HPP is higher than that of the BS at temperatures of 573 K or more. These results suggest that, when the HPP was employed, solid-liquid contact

happens even in film boiling region. Given the uncertainty of the measurements, differences observed in the maximum values of $-dT/dt$ were not sufficient to distinguish the CHF in these cases.

Figure 5 shows observation of wetting phenomena inside an HPP cells taken by a high-speed camera just after the start of cooling. The schematic diagram at the top of the figure depicts the test section used, which was accomplished by precisely cutting the HPP at the middle of wall and replacing the cropped part with a quartz glass tightly fixed. It can be seen that the liquid is absorbed into the HPP in a short time from the start of cooling, and that it reaches the heat-transfer surface within just 90 ms of experiment. Moreover, it only took approximately 1 s for the entire HPP to become completely wet.

<Figure 5>

Figure 6 shows the initial steady state temperature of the HPP and the stainless-steel rod measured using an infrared (IR) camera before being immersed. To make these measures, both were coated with a very thin layer of blackbody spray (emissivity of 0.94) from Ichinen Tasco Co, LTD specifically fabricated to permit accurate IR temperature measuring. The results indicated that when the temperature at TC1 was 639.7 K, the temperature of the heated surface was 624.2 K, and the HPP surface temperature was 452.7 K due to its low thermal conductivity (4 W/(mK)). Error in the measured interface temperatures is expected to be much smaller than the differences between the read temperatures.

<Figure 6>

The solid-liquid interface contact temperature T_{S-L} was calculated using the following equation:

$$T_{S-L} = \frac{(\rho ck)_S^{0.5} T_S + (\rho ck)_L^{0.5} T_L}{(\rho ck)_S^{0.5} + (\rho ck)_L^{0.5}} \quad (1)$$

where ρ is the density, c is the specific heat, k is the thermal conductivity, T_{S-L} is the interface temperature, and the subscripts S and L indicate the solid and liquid, respectively.

Using Equation 1, it was found that the temperature of the HPP surface when it contacts the saturated water was 434.9 K, and the temperature of the heated surface was 607.9 K. When the HPP touches the water, boiling occurs on it and its temperature rapidly decreases to 373 K.

To determine the degree of liquid-solid contact, the electrical resistance between the HPP and the heat-transfer surface was measured during additional quenching experiments. An electrode was placed on the HPP surface as shown in Figure 7, and the electrical resistance at a constant current of 0.3 mA was measured. The results showed that the electrical resistance is large when the stainless-steel rod is covered with a vapor film, but becomes smaller when solid-liquid contact occurs.

<Figure 7>

Figure 8 shows the change in the temperature and the electrical resistance as a function of time for one experiment (a) on the BS and (b) with the HPP. During film boiling, solid-liquid contact does not occur because the heated surface is covered with a vapor film and so a higher electrical resistance is observed. For the BS, after immersion of the test rod the electrical resistance was approximately 140 k Ω , which remained nearly constant during the film-boiling regime. It then decreased sharply as the transition to nucleate boiling occurred and reached 26 k Ω in the natural convection regime.

<Figure 8>

On the other hand, with the HPP, the initial electrical resistance was 40 k Ω during film boiling, which is much smaller than that of the BS case. It confirms that solid-liquid contact occurs locally from the start due to the presence of the HPP. The final resistance, in the single-phase region,

indicated by dashed lines in Figure 8, was almost the same found for the BS (approximately 27 k Ω). As shown in the inset in Figure 8(b), from 155 s to 160 s, in film boiling region, the electrical resistance fluctuates at a frequency of approximately 4 Hz, which corresponds to the frequency of large vapor bubbles detachment from the entire HPP structure.

Next, the NPDS with and without the HPP attached was tested. Figure 9 presents the effect of a TiO₂ nanocoating on the quenching curve and $-dT/dt$. Without an HPP, the quench time was 337 ± 65 s. When both NPDS and an HPP were used, the quench time was drastically reduced to approximately 50 ± 2 s, which is about 28-times smaller than that for the BS. This remarkable reduction in quench time can be attributed to the combination of water transport to the heated surface by capillary action in the HPP, and the vapor instability due to the NPDS. Results for $-dT/dt$ also suggested that the CHF was enhance in the last case.

<Figure 9>

Figure 10 compares images from the high-speed camera of film, transition and nucleate boiling mechanisms in BS and NPDS cases. The images show that when in film boiling the BS is completely covered by vapor blanket. On the NPDS, the vapor film became unstable and thus local solid-liquid contact, indicate by the red arrows, could be observed. The instability of the vapor film contributes to the shorter time until transition to nucleate boiling in this case.

<Figure 10>

It is well known that wettability and surface roughness can be changed by nanoparticle deposition [18–21]. In order to verify changes in the surface characteristics, a wettability test was carried-out. In this test, shown in Figure 11, a micro-syringe with a droplet of distilled water suspended at the tip of your needle was kept still in horizontal position and the surface to be tested was vertically elevated slowly until the droplet touched the surface. The spreading of the droplet of distilled water,

with approximately 2 μl of volume, was recorded at 500 frames per second and the wetted area as a function of time on the BS and the NPDS compared.

<Figure 11>

The results for the first 100 ms of recording are presented in Figure 12. The legend in the graphic also presents the final wetted area after 15 s for both cases.

<Figure 12>

It is notable that on the NPDS the water spread faster and the final wetted area was much larger than that of the BS. It indicates that both wettability and capillarity of the surface were greatly improved by the presence of the nanoparticles. These results could help to explain the shorter quenching time for the NPDS.

The change in surface roughness by the nanoparticles was checked with use of a copper cylinder. Although the material of the rod analyzed differs from that of the experiments, the purpose of this analysis is to qualitatively confirm that the presence of nanoparticles on the surface can increase its roughness. A BS and a NPDS were produced using the same procedures described for the stainless steel cylinder. The average roughness of these surfaces was also investigated using a 3D laser scanning confocal microscope (VK-X250, Keyence) with measurement accuracy of 0.2 μm . Four different areas (approximately 1.5 mm x 1.5 mm) of the surface were examined for the average roughness calculation. The results showed that the nanoparticles increased the roughness of the surface significantly. The average values found were $(2.4 \pm 0.1) \mu\text{m}$ and $(3.5 \pm 0.1) \mu\text{m}$ for the BS and NPDS respectively, what represents an increase of 46 % in the surface roughness.

4. CONCLUSIONS

Quenching experiments were conducted using a SUS304 stainless-steel rod with heated test surface of 30 mm in diameter at initial temperature of approximately 623 K, which was immersed in distilled water under saturated and atmospheric-pressure conditions. The main conclusions were as follows:

1. When an HPP is attached to the heated surface, the quench time is shortened by 6 times when compared to the case for a BS, due to liquid transport to the heated surface by capillary action in the HPP. Measurements of the electrical resistance between the HPP and the heated surface confirmed that the degree of liquid-solid contact was also increased.

2. A NPDS can make the vapor film become unstable and thus shorten the quench time. Analysis of this surface showed that its roughness, capillarity and wettability were increased by the presence of the nano-particles, increasing the chances of solid-liquid contact.

3. When the combination of an HPP and a NPDS was used, the quench time was reduced by 28 times compared to that for the BS. This was a consequence of the liquid being transported by capillary action through the HPP walls toward the heated surface where it spreads rapidly due to the presence of nanoparticles.

ACKNOWLEDGMENTS

The present study was supported in part by the Research Foundation for Electrotechnology of Chubu and the Initiatives for Atomic Energy Basic and Generic Strategic Research by the Ministry of Education, Culture, Sports, Science and Technology of Japan.

REFERENCES

- 1 [1] W. Ma, Y. Yuan, B.R. Sehgal, In-Vessel Melt Retention of Pressurized Water Reactors:
2 Historical Review and Future Research Needs, *Engineering*. 2 (2016) 103–111.
3 doi:10.1016/J.ENG.2016.01.019.
- 4 [2] L.W. Fan, J.Q. Li, D.Y. Li, L. Zhang, Z.T. Yu, Regulated transient pool boiling of water during
5 quenching on nanostructured surfaces with modified wettability from superhydrophilic to
6 superhydrophobic, *Int. J. Heat Mass Transf.* 76 (2014) 81–89.
7 doi:10.1016/j.ijheatmasstransfer.2014.04.025.
- 8 [3] J.Y. Kang, S.H. Kim, H. Jo, G. Park, H.S. Ahn, K. Moriyama, M.H. Kim, H.S. Park, Film
9 boiling heat transfer on a completely wettable surface with atmospheric saturated distilled
10 water quenching, *Int. J. Heat Mass Transf.* 93 (2016) 67–74.
11 doi:10.1016/j.ijheatmasstransfer.2015.09.049.
- 12 [4] I. Sher, R. Harari, R. Reshef, E. Sher, Film boiling collapse in solid spheres immersed in a
13 sub-cooled liquid, *Appl. Therm. Eng.* 36 (2012) 219–226.
14 doi:10.1016/j.applthermaleng.2011.11.018.
- 15 [5] A. Shahriari, M. Hermes, V. Bahadur, Electrical control and enhancement of boiling heat
16 transfer during quenching, *Appl. Phys. Lett.* 108 (2016). doi:10.1063/1.4943230.
- 17 [6] S.H. Hsu, Y.H. Ho, M.X. Ho, J.C. Wang, C. Pan, On the formation of vapor film during
18 quenching in de-ionized water and elimination of film boiling during quenching in natural sea
19 water, *Int. J. Heat Mass Transf.* 86 (2015) 65–71.
20 doi:10.1016/j.ijheatmasstransfer.2015.02.049.
- 21 [7] H. Lotfi, M.B. Shafii, Boiling heat transfer on a high temperature silver sphere in nanofluid,
22 *Int. J. Therm. Sci.* 48 (2009) 2215–2220. doi:10.1016/j.ijthermalsci.2009.04.009.
- 23 [8] H. Kim, G. DeWitt, T. McKrell, J. Buongiorno, L. wen Hu, On the quenching of steel and
24 zircaloy spheres in water-based nanofluids with alumina, silica and diamond nanoparticles,
25 *Int. J. Multiph. Flow.* 35 (2009) 427–438. doi:10.1016/j.ijmultiphaseflow.2009.02.004.
- 26 [9] S.Y. Chun, I.C. Bang, Y.J. Choo, C.H. Song, Heat transfer characteristics of Si and SiC
27 nanofluids during a rapid quenching and nanoparticles deposition effects, *Int. J. Heat Mass*

Transf. 54 (2011) 1217–1223. doi:10.1016/j.ijheatmasstransfer.2010.10.029.

[10] L.W. Fan, J.Q. Li, D.Y. Li, L. Zhang, Z.T. Yu, K.F. Cen, The effect of concentration on transient pool boiling heat transfer of graphene-based aqueous nanofluids, *Int. J. Therm. Sci.* 91 (2015) 83–95. doi:10.1016/j.ijthermalsci.2015.01.009.

[11] H. Kim, J. Buongiorno, L.W. Hu, T. McKrell, Nanoparticle deposition effects on the minimum heat flux point and quench front speed during quenching in water-based alumina nanofluids, *Int. J. Heat Mass Transf.* 53 (2010) 1542–1553. doi:10.1016/j.ijheatmasstransfer.2009.11.029.

[12] S. Mori, S. Mt Aznam, K. Okuyama, Enhancement of the critical heat flux in saturated pool boiling of water by nanoparticle-coating and a honeycomb porous plate, *Int. J. Heat Mass Transf.* 80 (2015) 1–6. doi:10.1016/j.ijheatmasstransfer.2014.08.046.

[13] S. Mt Aznam, S. Mori, A. Ogoshi, K. Okuyama, CHF enhancement of a large heated surface by a honeycomb porous plate and a gridded metal structure in a saturated pool boiling of nanofluid, *Int. J. Heat Mass Transf.* 115 (2017) 969–980. doi:10.1016/j.ijheatmasstransfer.2017.07.089.

[14] S. Mori, K. Okuyama, Enhancement of the critical heat flux in saturated pool boiling using honeycomb porous media, *Int. J. Multiph. Flow.* 35 (2009) 946–951. doi:10.1016/j.ijmultiphaseflow.2009.05.003.

[15] S. Mori, N. Maruoka, K. Okuyama, Critical heat flux enhancement by a two-layer structured honeycomb porous plate in a saturated pool boiling of water, *Int. J. Heat Mass Transf.* 118 (2018) 429–438. doi:10.1016/j.ijheatmasstransfer.2017.10.100.

[16] S. Mori, F. Yokomatsu, M. Tanaka, K. Okuyama, Rapid cooling of a high-temperature block by the attachment of a honeycomb porous plate on a nanoparticle-deposited surface, *Appl. Therm. Eng.* 133 (2018) 576–579. doi:10.1016/j.applthermaleng.2018.01.088.

[17] T.K. Kim, G. Cheol, H. Noh, H. Kim, H. Sun, Quenching experiments on various thermal properties under saturated and subcooled water condition with high-speed visualization, (2017) 2–5.

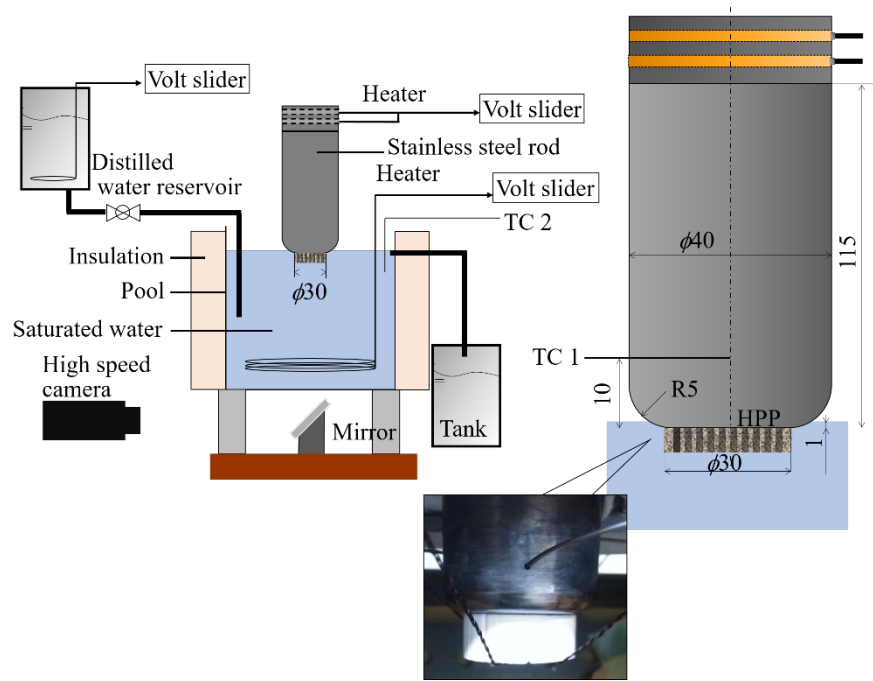
- 1 [18] S.G. Kandlikar, A Theoretical Model to Predict Pool Boiling CHF Incorporating Effects of
2 Contact Angle and Orientation, J. Heat Transfer. 123 (2001) 1071. doi:10.1115/1.1409265.
- 3 [19] Y. Takata, S. Hidaka, M. Masuda, T. Ito, Pool boiling on a superhydrophilic surface, Int. J.
4 Energy Res. 27 (2003) 111–119. doi:10.1002/er.861.
- 5 [20] H. Jo, S. Kim, H. Kim, J. Kim, M.H. Kim, Nucleate boiling performance on nano
6 microstructures with different wetting surfaces.pdf, (2012) 1–9.
- 7 [21] H. Jo, J.M. Kim, H. Yeom, G.C. Lee, H.S. Park, M. Kiyofumi, M.H. Kim, K. Sridharan, M.
8 Corradini, Boiling performance and material robustness of modified surfaces with multi scale
9 structures for fuel cladding development, Nucl. Eng. Des. 291 (2015) 204–211.
10 doi:10.1016/j.nucengdes.2015.04.032.

11

1 **FIGURES**

2

3



4

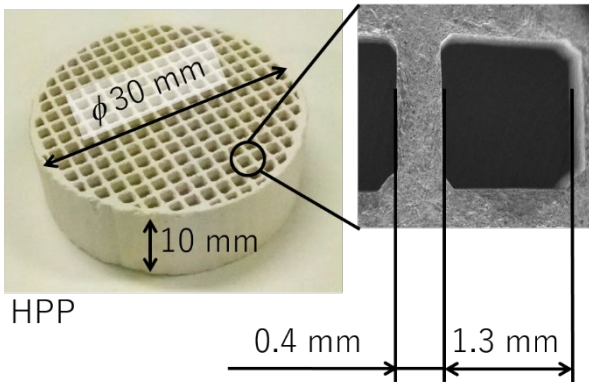
5

6 Figure 1 Schematic diagram of the experimental apparatus. All dimensions are presented in
7 millimeters.

8

9

10



11

12

Figure 2 Honeycomb porous plate (HPP).

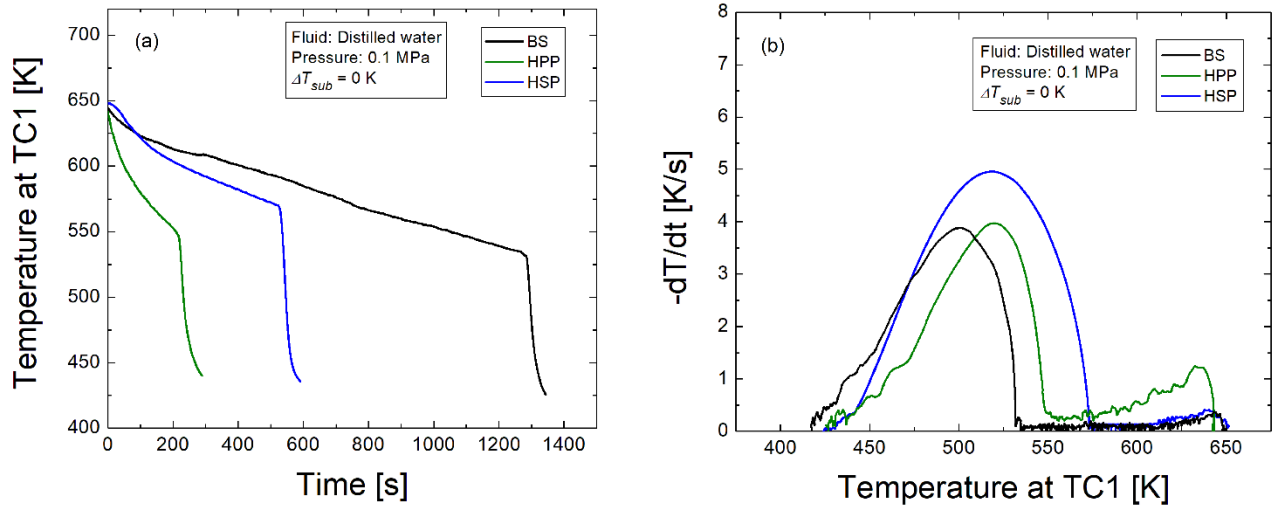
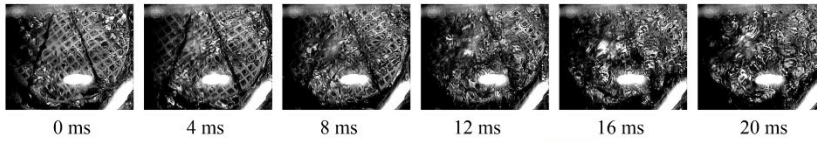
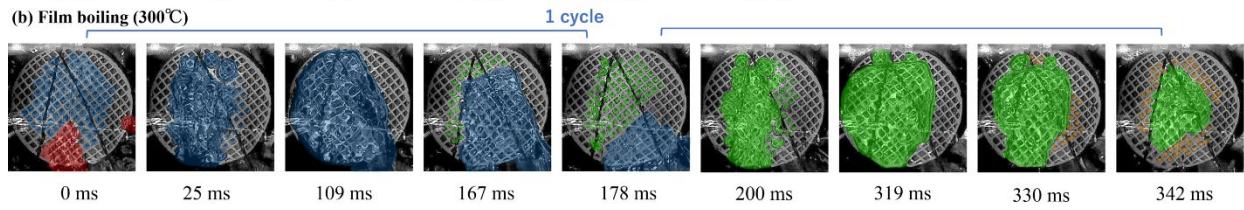


Figure 3 (a) Quenching curve, and (b) $-dT/dt$ at TC1 in the case of a BS, an HPP and an HSP.

(a) Immediately after starting cooling (370°C)



(b) Film boiling (300°C)



(c) Nucleate boiling (250°C)

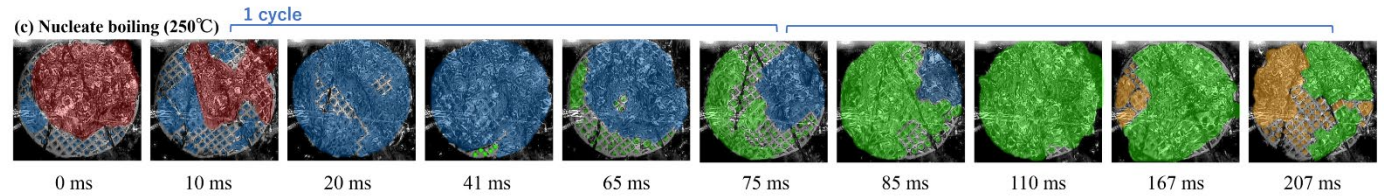


Figure 4 Boiling configuration and bubbles departure in the case of an HPP. Different colors represent different bubbles.

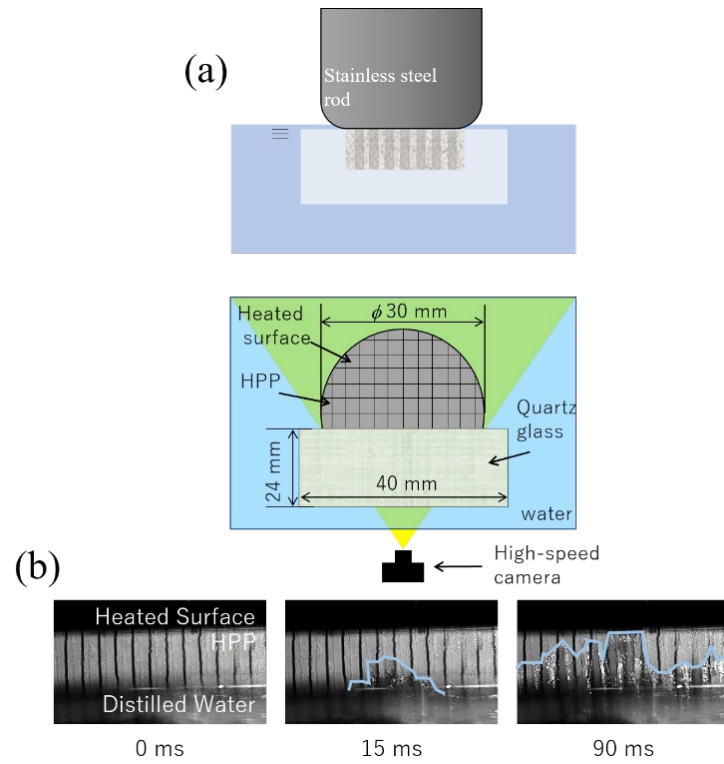


Figure 5 (a) Schematic diagram of the specimen, and (b) Visualization results the wetting phenomena inside the HPP immediately after the immersion at 0, 15, and 90 ms.

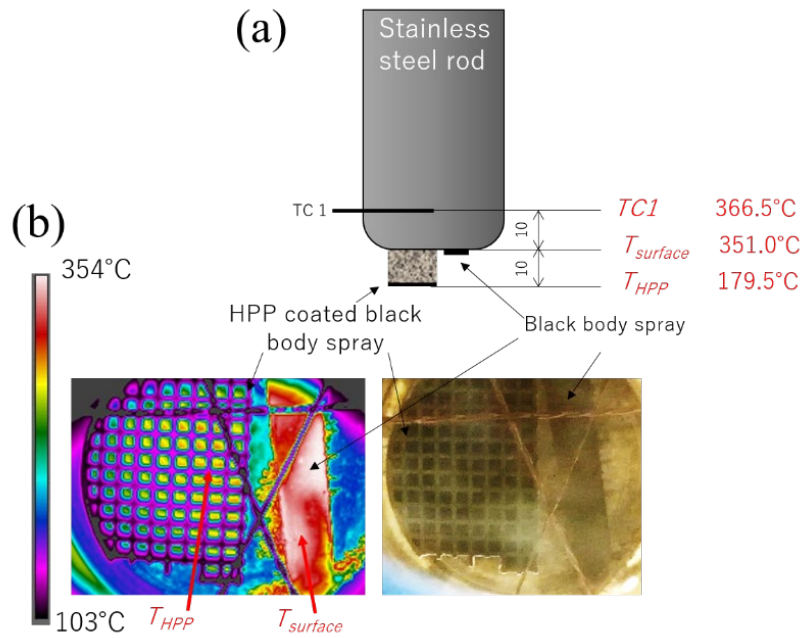


Figure 6 (a) Schematic diagram of the specimen, and (b) IR and optical images for surface temperature measurement.

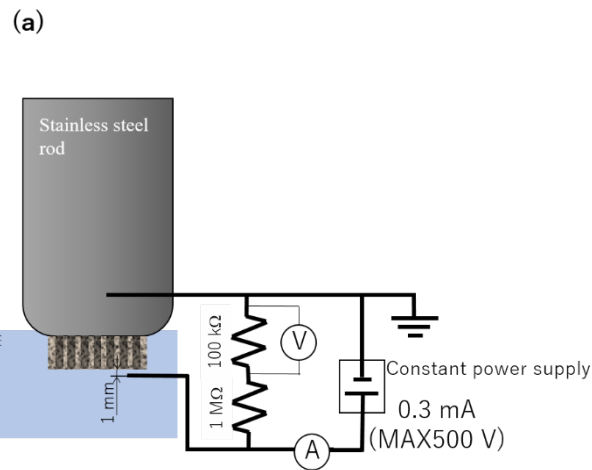


Figure 7 Schematic diagram of electrical circuit for detecting gas-liquid contact.

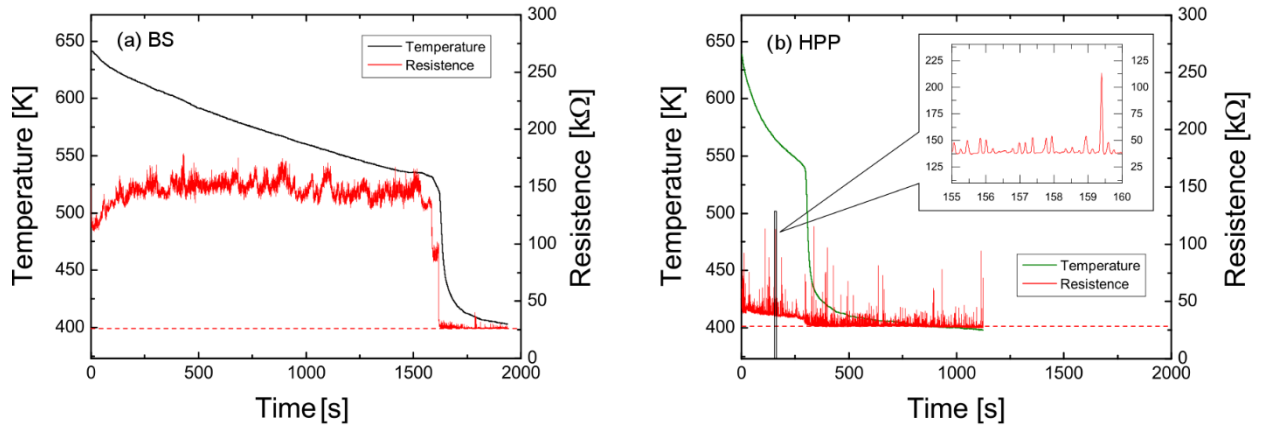


Figure 8 Quenching curve with resistance values depending on liquid-solid contact in the case of (a) BS, and (b) HPP.

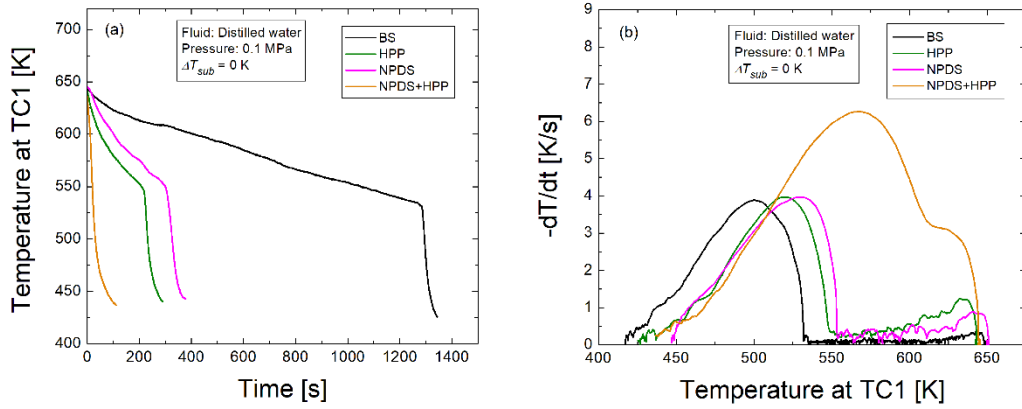


Figure 9 Quenching curve and $-dT/dt$ at TC1 in the case of a BS, an HPP, a NPDS, a NPDS+HPP.

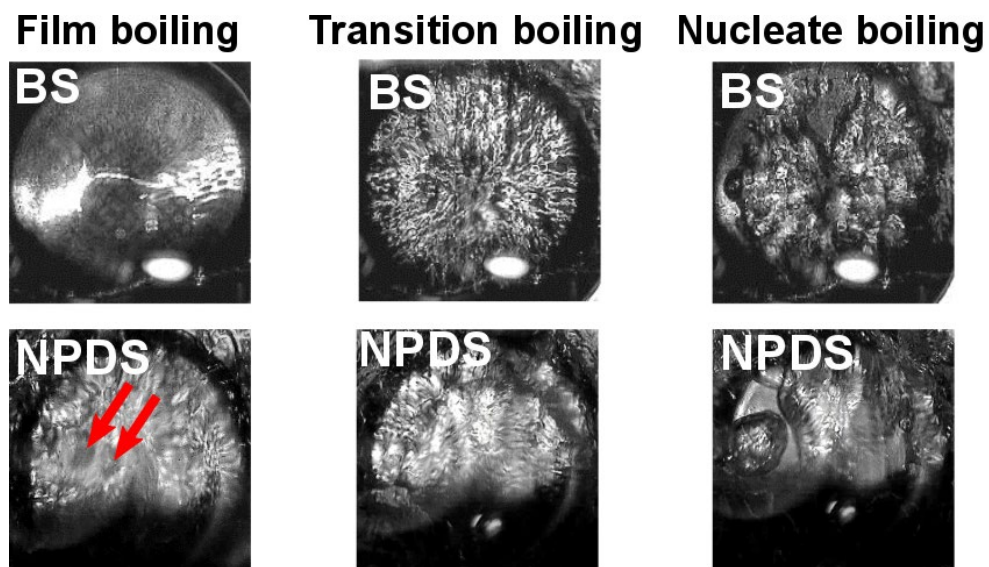


Figure 10 Images of film, transition and nucleate boiling on the BS and the NPDS. The red arrows show solid-liquid contact during film boiling on the NPDS.

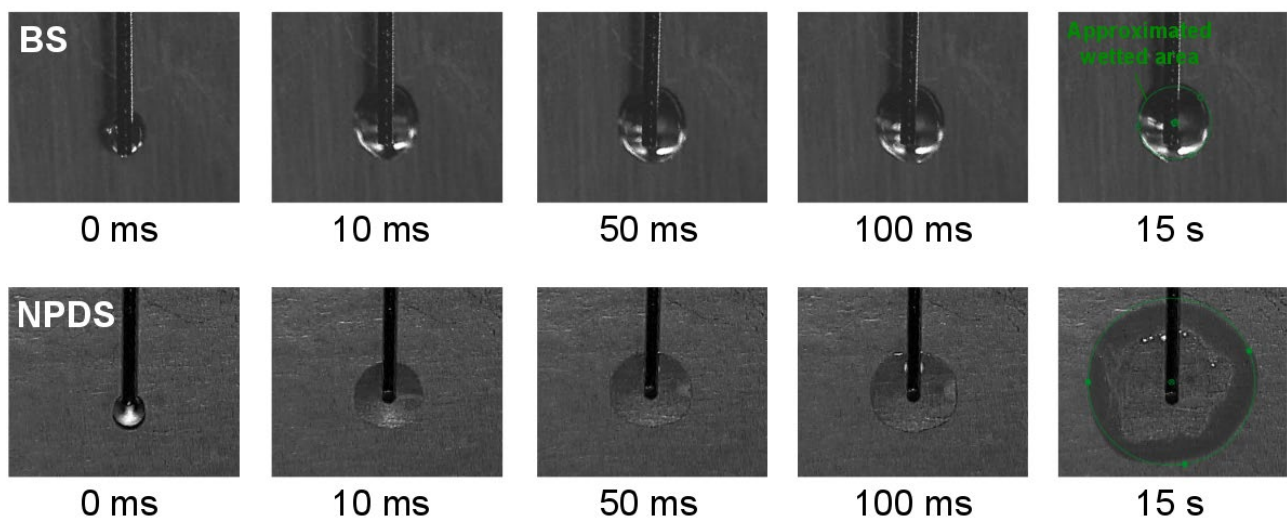


Figure 11 Wettability and capillarity test on the BS and the NPDS.

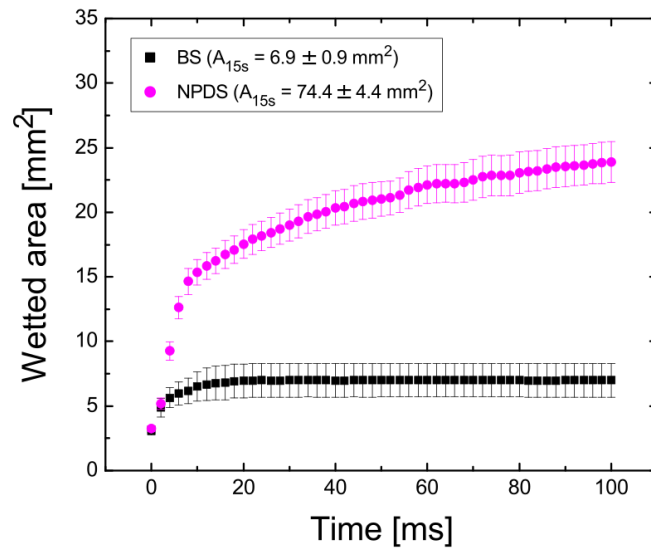


Figure 12 Wetted area as a function of time for the BS and the NPDS.

HIGHLIGHTS

- Quenching of a stainless steel rod with an honeycomb porous plate (HPP) attached to its lower surface was investigated.
- Experiments were conducted on a bare surface (BS) and a nanoparticle deposited surface (NPDS).
- Quenching time with the HPP was 6-times shorter than that of the BS.
- Combination of an HPP and NPDS provided a quenching time 28-times shorter than the BS.
- The shorter quenching time was attributed to the capillarity of the HPP and improvement of surface wettability by the nanoparticles.